

Central Lancashire Online Knowledge (CLoK)

Title	Interplay of large-scale drift and turbulence in the heliospheric propagation
	of solar energetic particles
Type	Article
URL	https://clok.uclan.ac.uk/id/eprint/54067/
DOI	https://doi.org/10.3847/1538-4357/ad9c3b
Date	2025
Citation	Laitinen, Timo Lauri mikael and Dalla, Silvia (2025) Interplay of large-scale drift and turbulence in the heliospheric propagation of solar energetic particles. The Astrophysical Journal, 979 (2). p. 106. ISSN 0004-637X
Creators	Laitinen, Timo Lauri mikael and Dalla, Silvia

It is advisable to refer to the publisher's version if you intend to cite from the work. https://doi.org/10.3847/1538-4357/ad9c3b

For information about Research at UCLan please go to http://www.uclan.ac.uk/research/

All outputs in CLoK are protected by Intellectual Property Rights law, including Copyright law. Copyright, IPR and Moral Rights for the works on this site are retained by the individual authors and/or other copyright owners. Terms and conditions for use of this material are defined in the http://clok.uclan.ac.uk/policies/

OPEN ACCESS



Interplay of Large-scale Drift and Turbulence in the Heliospheric Propagation of Solar Energetic Particles

T. Laitinen to and S. Dalla

Jeremiah Horrocks Institute, University of Central Lancashire, UK; tlmlaitinen@uclan.ac.uk
Received 2024 September 6; revised 2024 November 21; accepted 2024 December 7; published 2025 January 21

Abstract

The gradient and curvature of the Parker spiral interplanetary magnetic field give rise to curvature and gradient guiding-center drifts on cosmic rays (CRs). The plasma turbulence present in interplanetary space is thought to suppress the drifts; however, the extent to which they are reduced is not clear. We investigate the reduction of the drifts using a new analytic model of heliospheric turbulence where the dominant 2D component has both a wavevector and magnetic field vector normal to the Parker spiral, thus fulfilling the main criterion of 2D turbulence. We use full-orbit test-particle simulations of energetic protons in the modeled interplanetary turbulence, and analyze the mean drift velocity of the particles in heliolatitude. We release energetic proton populations of 10, 100, and 1000 MeV close to the Sun and introduce a new method to assess their drift. We compare the drift in the turbulent heliosphere to drift in a configuration without turbulence, and to theoretical estimates of drift reduction. We find that drifts are reduced by a factor 0.2–0.9 of that expected for the heliospheric configuration without turbulence. This corresponds to a much less efficient suppression than what is predicted by theoretical estimates, particularly at low proton energies. We conclude that guiding-center drifts are a significant factor for the evolution of CR intensities in the heliosphere, including the propagation of solar energetic particles in the inner heliosphere.

Unified Astronomy Thesaurus concepts: Solar energetic particles (1491); Heliosphere (711); Interplanetary magnetic fields (824); Interplanetary turbulence (830)

1. Introduction

The heliosphere is traversed by different populations of energetic charged particles, generally termed cosmic rays (CRs), with sources varying from the Sun and interplanetary space to outside the heliosphere in Galactic and extragalactic sources. The propagation of these particles is guided by the interplanetary magnetic field (IMF), which has the macroscopic shape of an Archimedean spiral, the Parker spiral, due to the magnetic field, originating from the rotating Sun, being frozen in the solar wind plasma (E. N. Parker 1958).

In the simplest approximation, the CRs propagate parallel to the Parker spiral magnetic field. However, the magnetic field is curved, and its magnitude depends on the heliocentric distance, thus the CRs are subject to gradient and curvature guiding-center drifts (e.g., J. A. Burns & G. Halpern 1968). The large-scale drifts influence the modulation of the intensities of galactic cosmic rays (GCRs) that propagate through the outer heliosphere to be observed at Earth (e.g., J. R. Jokipii et al. 1977). They also cause solar energetic particles (SEPs) to drift in latitude and longitude, and lose energy (e.g., S. Dalla et al. 2013, 2015; M. S. Marsh et al. 2013).

The large-scale IMF is superposed by a fluctuating component, which is due to the solar wind turbulence. This turbulent component causes field-line random walk (FLRW), resulting in CRs spreading stochastically across the large-scale average field. Further, the velocity vector of the CRs is affected by the turbulence, which results in scattering of the CRs along

Original content from this work may be used under the terms of the Creative Commons Attribution 4.0 licence. Any further distribution of this work must maintain attribution to the author(s) and the title of the work, journal citation and DOI.

the random-walking field lines (E. N. Parker 1965; J. R. Jokipii 1966).

The interplay between the effects of turbulence and the drift motion due to large-scale gradients and curvature has gained significant attention; however, the details of this interaction are not clear. For GCRs, large-scale drifts need to be suppressed within modulation models in order for the models to be able to reproduce observations (e.g., M. S. Potgieter et al. 1989). Several theoretical works have suggested that turbulence reduces large-scale drifts (e.g., L. J. Gleeson 1969; M. A. Forman et al. 1974; J. W. Bieber & W. H. Matthaeus 1997; J. Giacalone 1999; N. E. Engelbrecht et al. 2017; J. P. van den Berg et al. 2021), and reduction of drifts has found some support from full-orbit test-particle simulations of charged particles in synthetic turbulent magnetic fields (e.g., J. Giacalone 1999; J. Candia & E. Roulet 2004; J. Minnie et al. 2007; R. C. Tautz & A. Shalchi 2012). However, these theoretical works and simulation studies have used either a constant or gradient-only background magnetic field configuration; thus, possible suppression of CR drifts in a realistic heliospheric context has not been probed.

In this work, we investigate the effect of turbulence on guiding-center drifts of SEPs by means of 3D test-particle simulations including turbulence superposed on a Parker spiral IMF. We make use of our newly developed analytical model of composite plasma turbulence in the Parker spiral heliospheric configuration (T. Laitinen et al. 2023a). We compare the latitudinal drift of SEPs in a turbulent heliosphere to that in an IMF without turbulence (S. Dalla et al. 2013; M. S. Marsh et al. 2013). We compare the simulation results with the predictions of drift reduction models (J. W. Bieber & W. H. Matthaeus 1997; N. E. Engelbrecht et al. 2017), and discuss the implications of our results on theoretical models of drift reduction.

2. Methods

2.1. Theoretical Calculations of Drift Reduction

Stochastic transport models of CRs typically include the macroscopic drift of the charged particles in the diffusion tensor that is used to describe the diffusive propagation of CRs due to plasma turbulence. Within the assumption of an isotropic particle velocity distribution, the large-scale drift velocity v_d of a charged particle due to the gradient and curvature of the magnetic field \boldsymbol{B} can be written in the form of

$$\mathbf{v}_d = \frac{pv}{3q} \nabla \times \frac{\mathbf{B}}{B^2},\tag{1}$$

where p, v, and q are the moment, speed, and charge of the particle, respectively (e.g., B. Rossi & S. Olbert 1970). This can be written as

$$\mathbf{v}_d = \nabla \times \left(\frac{\mathbf{v}}{3}r_L\hat{e}_B\right) = \nabla \times \kappa_A\hat{e}_B,$$
 (2)

where $r_L = p/(qB)$ is the particle's Larmor radius, \hat{e}_B is the unit vector along the magnetic field \mathbf{B} , and $\kappa_A = \frac{v}{3} r_L$ is the so-called antisymmetric diffusion tensor. If we consider this form in conjunction with the diffusive flux term in transport equations, $\nabla \cdot (\kappa \cdot \nabla f) = \partial_i \kappa_{ij} \partial_j f$, where κ is the diffusion tensor defined in a coordinate system where the z-axis is aligned along the magnetic field, $\hat{e}_z \| \hat{e}_B$, the curl in Equation (2) is equivalent to including antisymmetric off-axis diffusion tensor elements $\kappa_{xy} = -\kappa_{yx} = \kappa_A$.

In order to calculate the effect of turbulence on drifts, J. W. Bieber & W. H. Matthaeus (1997) considered the Taylor-Green–Kubo (TGK) formalism (G. I. Taylor 1922; M. S. Green 1951; R. Kubo 1957), where the diffusion tensor is given as

$$\kappa_{ij} = \int_0^\infty dt \langle v_j(t_0) v_i(t_0 + t) \rangle = \int_0^\infty dt R_{ij}(t), \qquad (3)$$

where $\langle \rangle$ represents an ensemble average, and

$$R_{ii}(t) = \langle v_i(t_0)v_i(t_0+t)\rangle \tag{4}$$

is a correlation function that is statistically independent of t_0 . For a (positively) charged particle in a uniform magnetic field, the velocity components are $v_x = v_{\perp} \cos(\Omega t + \phi_0)$, $v_y = -v_{\perp} \sin(\Omega t + \phi_0)$, and $v_z = \text{constant}$, which results in the correlation functions

$$R_{xx} = R_{yy} = \frac{1}{2} v_{\perp}^2 \cos(\Omega t), \tag{5}$$

$$R_{yx} = -R_{xy} = \frac{1}{2}v_{\perp}^2 \sin(\Omega t), \qquad (6)$$

where $\Omega = v/r_L$ is the gyrofrequency of the particle. J. W. Bieber & W. H. Matthaeus (1997) assumed that because the turbulence disturbs the gyration of the charged particles, the correlation between the velocity components should include a decay term as follows:

$$R_{yx} = -R_{xy} = \frac{1}{2} v_{\perp}^2 \sin(\Omega t) e^{-t/\tau},$$
 (7)

where τ is the decorrelation timescale of the gyration. Using this expression for the correlation functions, by integration they

obtained the diffusion coefficients:

$$\kappa_{xx} = \kappa_{yy} = \frac{vr_L}{3} \frac{\Omega \tau}{1 + \Omega^2 \tau^2},\tag{8}$$

$$\kappa_{xy} = -\kappa_{yx} \equiv \kappa_A = \frac{vr_L}{3} \frac{\Omega^2 \tau^2}{1 + \Omega^2 \tau^2},\tag{9}$$

where an average over the pitch angle has been carried out. Comparing this form to the definition of κ_A in Equation (2), we see that the decorrelation of the particle velocity at timescale τ reduces the drift coefficient by a factor

$$f_s = \frac{\Omega^2 \tau^2}{1 + \Omega^2 \tau^2},\tag{10}$$

termed the drift reduction factor.

The question, then, is what is the correct timescale for the decorrelation of the particle gyromotion to be used to evaluate f_s ? J. W. Bieber & W. H. Matthaeus (1997) approached the question by assuming that the gyromotion decorrelates when the particles, following diffusing field lines, have drifted the distance of their gyroradius from their original position across the mean field direction. Following this argument, they arrived at an expression:

$$\Omega \tau = \frac{2r_L}{(3D_1)},\tag{11}$$

where D_{\perp} is the magnetic field-line diffusion coefficient. Thus, the drift reduction coefficient depends on the turbulence amplitude, its associated length scales (e.g., W. H. Matthaeus et al. 1999), as well as the particle energy and mass-to-charge ratio.

Using a similar approach, N. E. Engelbrecht et al. (2017) and J. P. van den Berg et al. (2021) considered that the relevant cross-field scale for the decorrelation should be the perpendicular mean free path of the particles, λ_{\perp} . They further assumed that the particle cross-field velocity is determined by random walk of the field lines, arriving at

$$\Omega \tau = \frac{r_L}{\lambda_{\parallel}} \frac{B_0}{dB},\tag{12}$$

where dB^2 is the variance of the turbulence.

It should be noted that the derivation of Equation (9) does not involve large-scale gradients; it is conducted with the assumption of a uniform magnetic field. Thus, it does not describe the large-scale drifts or their reduction; rather, it describes the asymmetric flux of particles due to their disturbed gyration.

It should also be noted that in the limit $\tau \to \infty$, κ_A cannot be defined by this approach, as the integral in Equation (3) is not defined.

2.2. Test-particle Simulations

Drift reduction due to turbulence has been studied by several researchers by means of full-orbit test-particle simulations (e.g., J. Giacalone 1999; J. Candia & E. Roulet 2004; J. Minnie et al. 2007; R. C. Tautz & A. Shalchi 2012). These works typically superpose homogeneous turbulence on a constant-background magnetic field, a configuration that is similar to that used in the theoretical models presented in Section 2.1. In such a configuration, measuring the macroscopic drift of a particle population cannot be used to analyze drift or its reduction, as

the macroscopic drift requires a gradient or curvature in the macroscopic field. Instead, these studies use the approach suggested by J. Giacalone (1999), where $\kappa_{ij} = \langle v_i \Delta r_j \rangle$, with v_i and Δr_j the i and j components, respectively, of velocity and spatial displacement normal to the background magnetic field. Only J. Minnie et al. (2007) used simulations where the background magnetic field has a gradient and macroscopic drifts are present. We shall return to these simulations in Section 4.

For this work, we analyze IMF guiding-center drift by integrating the full equation of motion for charged particles in the heliosphere via the simulation framework developed by S. Dalla & P. K. Browning (2005) and M. S. Marsh et al. (2013). The IMF is formed of a Parker spiral magnetic field superposed with turbulent fluctuations, as presented in T. Laitinen et al. (2023a). It should be noted that, in the present work, the model is monopolar, in the form of

$$\boldsymbol{B} = A B_0 \frac{r_0^2}{r^2} \left[\hat{\boldsymbol{e}}_r - \frac{r}{a} \hat{\boldsymbol{e}}_\phi \right], \tag{13}$$

where A is the sign of the magnetic field, $a = v_{\rm sw}/(\Omega_{\odot} \sin \theta)$, with $v_{\rm sw}$ and Ω_{\odot} the solar wind speed and solar rotation rate, respectively, $B_0 \approx B(r_0)$ when $r_0 \ll a$, with r_0 a reference location close to the Sun, and θ the colatitude. Thus, our present work does not include the effects of the heliospheric current sheet (M. Battarbee et al. 2017, 2018). We denote the polarity of the IMF with "B+" for an IMF pointing away from the Sun, with A=1, and "B-" for an IMF pointing toward the Sun, with A=-1. From the equation for magnetic drift (Equation (1)), it is clear that the drift velocity changes its direction with different IMF polarities. We note that the model used in the present work also does not include the convectional or turbulent electric field, thus the corotation drift and deceleration of CRs are not present in the simulations.

For the turbulence in our model, we use the heliospheric analytic 2D-slab composite turbulence model model described in T. Laitinen et al. (2023a). The model consists of a 2D turbulence component which is transverse with respect to the Parker spiral, and has a fluctuating magnetic field $\delta \boldsymbol{B}$ normal to the Parker spiral everywhere. The 2D component is complemented with a weaker slab-like component, which is dominated by radial slab modes close to the Sun, and is azimuthal at larger distances. The turbulence is realized as a sum of Fourier modes following the approach of J. Giacalone & J. R. Jokipii (1999), with 128 each of slab and 2D-mode waves, which are used to calculate the magnetic field at the particle location. Note that this approach differs from approaches where the turbulent magnetic field is precalculated on a 3D grid using a Fourier transform; in such cases, the simulation domain is limited by the largest scales included in the turbulence spectra. We refer to simulations performed with this model as the "turbulence" model throughout the rest of the manuscript.

We compare results from the turbulence model to heliospheric particle simulations without superposed turbulence. To do so, we run simulations using the approach presented in M. S. Marsh et al. (2013), where the particles are traced with full 3D test-particle simulations in Parker spiral geometry, with \boldsymbol{B} given by Equation (13) without turbulent field-line meandering. In these simulations, the effect of the turbulence on the particles is modeled as scattering events where the particle's velocity vector is scattered at random times, parameterized by a

constant parallel scattering mean free path, λ_{\parallel} (M. S. Marsh et al. 2013). We refer to these simulations as the "scatter" model. Note that cross-field scattering is not explicitly implemented in the scatter model: The only cross-field motion is caused by large-scale drifts and the random walk of the particle gyrocentre as the velocity vector is randomized. For the scatter and turbulence approaches to be comparable, we have used a parallel mean free path according to standard quasilinear theory (SQLT; e.g., J. R. Jokipii 1966) derived from the turbulence model parameters used in the turbulence runs. As the obtained SQLT mean free path varies with radial distance from the Sun, we average its value over distances from $2r_{\odot}$ to 1 au.

In this work, we simulate energetic protons at different proton energies and interplanetary space conditions. For each parameter set, we simulate 1000 particles in 100 different turbulence realizations, with the turbulence mode phases and polarizations differing in each realization, thus giving a total of 100,000 particles for each simulation set. The particles are injected at $2r_{\odot}$ heliocentric distance at the solar equator, with an isotropic velocity distribution, and their propagation in the heliosphere is traced for 48 hr. The parameters of the eight simulation sets are given in Table 1, with each set including both a turbulence and a scatter simulation run (column (5)). We simulate energetic protons from nonrelativistic to relativistic energies, at 10, 100, and 1000 MeV (column (2) in Table 1), for the two polarities of the monopolar IMF (column (3)). The relative turbulence amplitude at 1 au used in the turbulence simulations is given in column (7) of Table 1, with the corresponding scattering mean free path used in the scattering simulations given in column (6). Other turbulence parameters are as in T. Laitinen et al. (2023b), briefly described in Appendix A.

2.3. Determining the Latitudinal Drift Velocity

Previous studies have derived drift coefficients in a uniform background magnetic field with homogeneous turbulence. In this type of configuration, the coefficients do not depend on the particle location, thus the analysis methods can average particle statistics over the entire simulation volume. In our heliospheric configuration, however, use of such methods is not possible: Turbulence characteristics, and thus also the particle transport parameters, depend significantly on heliospheric location (e.g., R. Chhiber et al. 2017). Drift velocities also vary significantly with particle location (e.g., S. Dalla et al. 2013). Thus, the coefficients obtained by averaging over the simulation volume (by tracing particles through the entire heliosphere) would not represent the coefficients at any given location, but an average value over the whole heliosphere. To alleviate this issue, and produce coefficients for our turbulence and scatter particle simulations that can be compared with each other, we have developed a new methodology to analyze the drift experienced by the particles.

Our method is based on the fundamental difference between the effects of the two distinct physical processes (turbulence and drift) on the particle distribution. We initialize our particles around the solar equator, at $\theta = \pi/2$. Our turbulence model is symmetric in latitude, thus any asymmetry in the distribution in latitude with respect to the solar equator cannot be caused by the stochastic turbulence; without drift, the mean of the particle distribution in colatitude would remain at $\theta = \pi/2$. On the other hand, in a unipolar field, drift in heliolatitude causes

Table 1
Parameters of the Simulation Runs

Set	E_k (MeV)	Pol	$v_{d\theta,\text{theor}} (\text{km s}^{-1})$	Sim.	λ_{\parallel} (au)	dB^2/B^2	$\frac{\langle v_{d\theta} \rangle_r}{(\text{km s}^{-1})}$	$\frac{\sigma}{(\text{km s}^{-1})}$
1	10	B+	17.	Scat.	0.37		14.	0.38
				Turb.		0.60	3.5	19.
2	10	B-	17.	Scat.	0.37		-14.	0.39
				Turb.		0.60	-4.7	17.
3	100	$\mathrm{B}+$	160.	Scat.	1.6		110.	2.2
				Turb.		0.20	110.	81.
4	100	$\mathrm{B}+$	160.	Scat.	0.55		120.	2.3
				Turb.		0.60	82.	64.
5	100	B+	160.	Scat.	0.17		130.	3.3
				Turb.		2.00	40.	58.
6	100	B-	160.	Scat.	0.55		-120.	2.6
				Turb.		0.60	-82.	53.
7	1000	$\mathrm{B}+$	1300.	Scat.	0.87		840.	18.
				Turb.		0.60	780.	300.
8	1000	B-	1300.	Scat.	0.87		-840.	18.
				Turb.		0.60	-800.	300.

Note. Column (1): the set identifier for the runs, with the rows for the scatter and turbulence simulation runs within the sets indicated in column (5). Column (2): the proton energy. Column (3): the magnetic field polarity. Column (4): the theoretical $v_{d\theta \text{ theor}}$, as calculated in Appendix B. Columns (6) and (7): the parallel scattering mean free path and turbulence variance at 1 au heliocentric distance, used for the scatter and turbulence simulations, respectively. Columns (8) and (9): the $\langle \overline{v_{d\theta}} \rangle_r$ and the uncertainty σ , obtained from the distributions shown in Figure 3.

particles to propagate systematically either northwards or southwards depending on the magnetic field polarity (*A* in Equation (13); S. Dalla et al. 2013). Thus, we consider the broadening of the particle distribution to be caused by turbulence, and any changes in the mean latitude of the particle distribution to be caused by large-scale drifts.

To analyze the latitudinal propagation of a particle, we consider its first and last crossing of the 1 au sphere, taking place at times t_f and t_l , respectively. The change in colatitude between the two crossings is

$$\Delta \theta = \theta_I - \theta_f \tag{14}$$

and the time interval between the crossings is

$$\Delta t = t_l - t_f. \tag{15}$$

The latitudinal velocity of the particle averaged between the first and last 1 au sphere crossing, $v_{d\theta}$, can be then defined as

$$v_{d\theta} = r_e \frac{\Delta \theta}{\Delta t},\tag{16}$$

where $r_e = 1$ au. It should be noted that $v_{d\theta}$ does not represent the 1 au value of the latitudinal velocity; rather, it is the average latitudinal velocity of the particle over its entire trajectory in the heliosphere between t_f and t_l .

We use the interval between the first and the last crossing instead of intervals between consecutive crossings in our definitions to avoid giving larger statistical weight to individual particles that cross the 1 au sphere multiple times. Our method also ignores the initial propagation of the particles in the near-Sun region where the stochastic spreading of the particle population is strong; as discussed in T. Laitinen et al. (2023a), the field-line meandering in such an environment can cause large local deviations. We further exclude particles for which $\Delta t < 100\,\mathrm{s}$, large compared to $\Omega = 0.49\,\mathrm{s}^{-1}$ at 1 au (for nonrelativistic particles), to avoid effects of the Larmor radius of the particles on $\Delta\theta$.

Figure 1(a) shows the distribution of $\Delta\theta$ values for 100 MeV protons (filled contours). Here, the entire population of 100,000 protons over the 100 turbulence realizations is used. The particles with small Δt have returned to 1 au soon after their initial crossing, and have subsequently escaped to further distances without returning. Particles with larger Δt display a wider distribution in $\Delta\theta$. This is due to the particles decoupling from their original meandering field line to different field lines at later times. This stochastic process can result in a particle's final crossing of the 1 au sphere to be up to 90° from their initial crossing colatitude.

To investigate the temporal evolution of $\Delta\theta$, we divide the Δt axis into bins and calculate median values of $\Delta\theta$ over the particle population in each bin, indicated as $\overline{\Delta\theta}(\Delta t)$. We show $\overline{\Delta\theta}$ as a function of Δt in Figure 1(b) with red crosses. As can be seen, $\overline{\Delta\theta}$ increases systematically, demonstrating a macroscopic, systematic drift of the particle population in time.

We compare the drift in Figure 1(b) to the theoretical drift. The theoretical drift velocity (Equation (B3)) is given in column (4) of Table 1, following the derivation presented in Appendix B. The dashed black curve in Figure 1 shows the change in colatitude of a particle obeying the theoretical drift as

$$\Delta \theta_{\text{theor}} = v_{d\theta \text{ theor}} \Delta t. \tag{17}$$

As can be seen, the $\overline{\Delta\theta}$ follows the trend of the theoretical prediction well, however at slightly lower values.

To further analyze the drift in velocity units, we calculate the median drift speed $\overline{v_{d\theta}}(\Delta t)$ and present it in units of $v_{d\theta \text{ theor}}$ in Figure 1(c). As can be seen, $\overline{v_{d\theta}}(\Delta t)$ is of the same order as $v_{d\theta \text{ theor}}$, but lower in magnitude, reaching its maximum value of 0.85 $v_{d\theta \text{ theor}}$ at $\Delta t \approx 10,000 \text{ s}$.

It should be emphasized that the wide, temporally widening extent of the $\Delta\theta$ distribution seen in Figure 1(a) cannot be considered as an uncertainty of $\overline{\Delta\theta}$. The extent of the distribution arises from the decoupling of the particles from the stochastically meandering field lines: It is a measurable quantity that describes the turbulence-induced stochastic particle propagation. The wide extent is a result of a physical

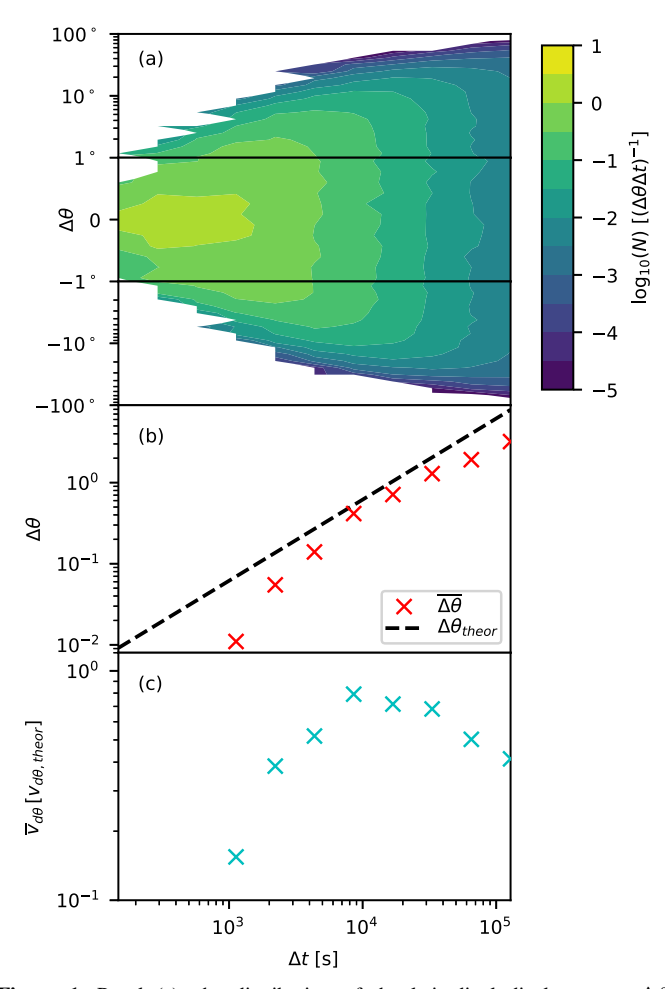


Figure 1. Panel (a): the distribution of the latitudinal displacements $\Delta\theta$ between the first and last 1 au crossing of 100 MeV protons (simulation set 4) as a function of the time Δt between the first and last crossing, ensemble-averaged over all turbulence realizations (note that the interval of $\Delta\theta \in [-1, 1]$ on the vertical axis is linear). Panel (b): the red crosses in the top panel show $\overline{\Delta\theta}$, and the dashed line the theoretical $\Delta\theta$ due to guiding-center drifts (see Appendix B). Panel (c): the drift velocity $\overline{Vd\theta}$ in units of the theoretical velocity.

process that is distinct from the large-scale systematic drifts which are caused by large-scale gradients and curvature of the Parker spiral.

In the next section, we use our new methodology to investigate the dependence of the drift velocity on the particle energy and turbulence amplitude, as well as its temporal evolution and variation across different turbulence realizations. For the latter, it is useful to consider the distribution of the median drift velocities over the 100 realizations. The median drift velocity over realization r, and over all Δt values, is indicated as $\langle v_{d\theta} \rangle_r$.

3. Results

3.1. Drifts from Test-particle Simulations

We first investigate the temporal evolution of $\overline{v_{d\theta}}(\Delta t)$ in Figure 2 for simulation sets 4 and 6 in panels (a) and (b), respectively, in units of the theoretical drift velocity. In the figure, the cyan and magenta symbols depict $\overline{v_{d\theta}}(\Delta t)$ for the turbulence simulations, and the solid cyan curve the same for the scatter simulation sets 4 and 6. Note that the binning in Δt

is linear, unlike in Figure 1(c) where we used logarithmic binning.

As can be seen, both the turbulence and scatter simulations attain $\overline{v_{d\theta}}(\Delta t)$ values with the same sign as the polarity used in the simulation set. The drift from the scatter simulations is initially of the same order as $v_{d\theta,\text{theor}}$ (i.e., values 1 and -1 in Figures 2(a) and (b), respectively), however it decreases for larger Δt . This is caused by the particle propagation not being limited to the vicinity of 1 au where the theoretical drift velocity is calculated. As the particles propagate and spread into the inner and outer heliosphere before returning to 1 au, they sample heliocentric distances where the angular drift velocity is smaller than at 1 au (see Figure 7(b)). As a result, their integrated drift velocities between the first and last crossing are smaller than the 1 au values. This effect is evident in that for the particles with larger Δt , the deviation of the drift speed from the theoretical value at 1 au is progressively larger. For further details, see Appendix B.

The $\overline{v_{d\theta}}(\Delta t)$ from turbulent simulations is smaller in magnitude than the one from scatter simulations, and likewise is smaller for larger Δt . Thus, it appears that some reduction of drift is present in the turbulence simulations as compared to the scatter simulations. There is considerable statistical fluctuation, due to the different travel histories of the particles within the simulations.

In order to evaluate the effect of different turbulence realizations on the drift velocity obtained from our simulations, we show the distributions of $\langle v_{d\theta} \rangle_r$ in Figure 3 for the three proton energies used in this study for the moderate-turbulence case of $dB^2/B^2=0.6$ at 1 au, with the positive (B+) and negative (B-) magnetic polarity simulations shown by cyan and magenta symbols and lines, respectively. The crosses and horizontal error bars show the ensemble median $\overline{\langle v_{d\theta} \rangle_r}$ and the standard deviation σ over the distribution of $100 \langle v_{d\theta} \rangle_r$ values for the turbulence realizations. The values are given in Table 1 in the last two columns on lines denoted "Turb."

For comparison, we show in Figure 3 the $\langle v_{d\theta} \rangle_r$ for the scatter simulations with filled circle symbols. The standard deviations of the scatter simulations are smaller than the symbol size. The value of $v_{d\theta,\text{scat}}$ and the corresponding standard deviation are shown in the last two columns of Table 1 on lines denoted "Scat."

As we can see in Figure 3, the distributions of median drifts for the B+ and B- polarities have different signs, and for the higher energies the $v_{d\theta,\text{turb}}$ distributions for the different polarities are clearly distinct. For the 10 MeV protons, the distributions do overlap significantly, however the median values of the distributions differ and are of different sign, as expected. In addition, we performed a Kolmogorov-Smirnoff test, which confirmed that the B+ and B- distributions are statistically different even for the 10 MeV protons. In all the cases depicted in Figure 3 and in Table 1, the drift obtained with the scatter simulations is larger than $\langle v_{d\theta} \rangle_r$.

The theoretical drift velocity, shown in column (4) of Table 1, is of similar order as the scatter simulation drift; however, there are some differences. This is due to the fact that the theoretical value is valid only for particles at 1 au, whereas the simulated particles propagate in the IMF where the drift rate varies with heliocentric distance (see Figure 7(b)) and colatitude.

3.2. Drift Reduction Factor

To evaluate the effect of the turbulence on drifts, we compare the $\overline{v_{d\theta}}(\Delta t)$ obtained with turbulence simulations with

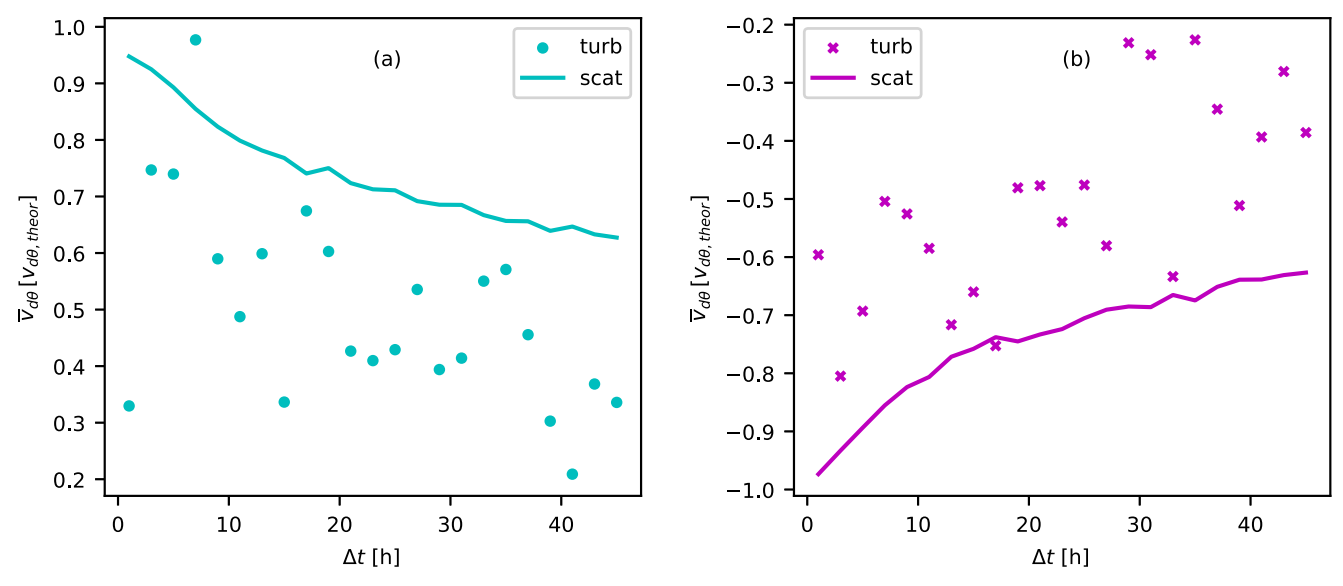


Figure 2. The drift velocity $v_{d\theta}$ (in units of the theoretical drift velocity; Equation (B3)) of 100 MeV protons in moderate turbulence for (a) B+ polarity (simulation set 4) and (b) B- polarity (simulation set 6) protons as a function of time interval Δt between the first and last 1 au crossing.

the drift expected without turbulence. As discussed above, $v_{d\theta, \text{theor}}$ calculated in Appendix B is limited to a specific heliospheric location. For this reason, we choose the drift from the scatter simulations as the reference drift without turbulence. This assumption can be justified by considering the form of Equation (10) which approaches unity for $\Omega \tau \gg 1$. For the scatter model, we can consider the decorrelation timescale τ to be equal to the parallel scattering time $t_{\text{scat}} = \lambda_{\parallel}/v$ (M. S. Marsh et al. 2013), which for all of our parameters are much larger than $1/\Omega$.

Under this assumption, we obtain the drift reduction coefficient by fitting the time-dependent $v_{d\theta,\text{turb}}$, as shown in Figure 2 as

$$v_{d\theta,\text{turb}} = f_s \ v_{d\theta,\text{scat}},$$
 (18)

where f_s is the drift reduction factor. We note that the number of crossings also depends on Δt , thus we fit Equation (18) weighting the turbulence simulation points with the number of particles. We perform the fit using the curve_fit function of the Python SciPy package (P. Virtanen et al. 2020). We show an example fit in Figure 4, where panel (a) shows the turbulence and scattering simulation $\overline{v_{d\theta}}(\Delta t)$ with cyan circles and line for 100 MeV protons (simulation set 4), respectively, and the fit to Equation (18) with a black dashed curve. In panel (b), the blue curve shows the number of particles used as weights for the fitting. As can be seen in panel (b), the number of 100 MeV protons used in the fitting decays as a function of Δt , thus, due to weighting, the low- Δt $\overline{v_{d\theta}}(\Delta t)$ affects the fit more strongly than the high- Δt $\overline{v_{d\theta}}(\Delta t)$.

The drift reduction factors and their standard deviations obtained from the fitting procedure are shown in the fifth and sixth columns of Table 2. We demonstrate the dependence of f_s on the relative amplitude of turbulence and proton energy in Figures 5 and 6, respectively, for the B+ polarity.

For comparison, we have also calculated the theoretical reduction factors from the models by J. W. Bieber & W. H. Matthaeus (1997) and N. E. Engelbrecht et al. (2017) using Equations (10)–(12). The field-line diffusion coefficient and particle cross-field diffusion coefficient required for these

were calculated using the random ballistic decorrelation (RBD) approach by M. C. Ghilea et al. (2011) and D. Ruffolo et al. (2012), respectively. These values are shown in columns (7) and (8) of Table 2. A comparison of these drift reduction factors is also shown in Figures 5 and 6. As can be seen, our reduction factor is considerably larger than that predicted by the theoretical approach, except for high energies and low turbulence amplitudes.

We note that care should be taken in comparing simulations with the TGK approach, as the simulation timescales should be much larger than the decorrelation timescale τ for TGK to be applicable. We can estimate the validity of the TGK approach by using the theoretical f_s values presented in Table 2, where all f_s values are at or below 0.90. Using Equation (10), $f_s < 0.90$ corresponds to $\tau\Omega > 3$, which, with the (nonrelativistic) gyrofrequency at 1 au being $\Omega = 0.49~{\rm s}^{-1}$ for our simulations, corresponds to $\tau \approx 6~{\rm s}$. As we exclude particles with $\Delta t < 100~{\rm s}$ from our analysis, we can conclude that for all our simulations $\Delta t \gg \tau$, and the TGK approach is valid.

We also show the drift reduction coefficients obtained from full-orbit particle simulations by J. Minnie et al. (2007) and R. C. Tautz & A. Shalchi (2012), who give the energy of particles in terms of $r_L/l_{b\parallel}$, where $l_{b\parallel}$ is the largest scale of the inertial scale of the slab spectrum, which for our turbulence model is $l_{b\parallel}=0.27$ au at r=1 au (T. Laitinen et al. 2023a). J. Minnie et al. (2007) used values $r_L/l_{b\parallel}=0.1$ and 1, which correspond to proton energies of 227 and 6040 MeV, whereas R. C. Tautz & A. Shalchi (2012) only used $r_L/l_{b\parallel}=0.1$. We give the $r_L/l_{b\parallel}$ for our simulations in column (3) of Table 2. As can be seen in Figure 5, the dependence of our drift reduction factor on the turbulence amplitude is similar to that obtained by J. Minnie et al. (2007) and R. C. Tautz & A. Shalchi (2012). The dependence of our drift on energy differs more significantly, particularly from the R. C. Tautz & A. Shalchi (2012) result (Figure 6), however this can be explained by the fact that the relative turbulence variance dB^2/B^2 is 1 in their

¹ Note that the reduction factor of N. E. Engelbrecht et al. (2017) depends strongly on the choice of the theory used to calculate the perpendicular diffusion coefficient; see J. P. van den Berg et al. (2021).

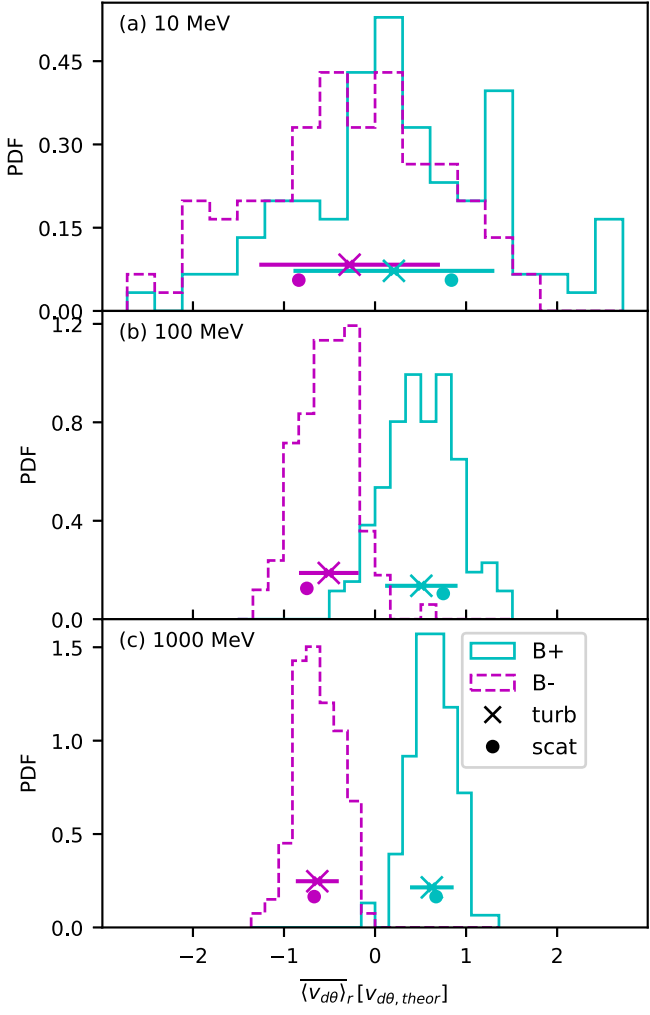


Figure 3. Probability density of $\langle v_{d\theta} \rangle_r$, the medians of the $v_{d\theta}$ of the 100 different turbulence realizations, for $dB^2/B^2=0.6$ at 1 au for (a) 10 MeV, (b) 100 MeV, and (d) 1000 MeV protons, in units of $v_{d\theta,\text{theor}}$. The cyan and magenta curves show the $\langle v_{d\theta} \rangle_r$ distributions for the B+ and B- polarities, respectively. The crosses and horizontal error bars show the median and uncertainty for the turbulence simulations, and the filled circles show the median for the scatter simulations.

work, whereas our simulations in Figure 6 have $dB^2/B^2 = 0.6$ at 1 au. By estimating the effect of the turbulence amplitude on f_s in Figure 5, it is clear that reducing the turbulence amplitude in the J. Minnie et al. (2007) and R. C. Tautz & A. Shalchi (2012) simulations would increase f_s considerably.

Thus, we can conclude that our simulations are well in line with the previous simulation work. It should be noted, though, that the simulations of J. Minnie et al. (2007), R. C. Tautz & A. Shalchi (2012), and ours in the present paper are not directly comparable, as the particle and turbulence parameters in the studies are different, and we use heliospheric magnetic field whereas the J. Minnie et al. (2007) and R. C. Tautz & A. Shalchi (2012) use constant-background magnetic field. We discuss these issues further in Section 4.

4. Discussion

In this work, we have investigated the effect of turbulence on large-scale guiding-center drifts of SEPs by using full-orbit test-particle simulations. We presented a methodology to evaluate the drift in latitude in turbulent heliospheric simulations, and compared it with simulations not including turbulence. We derived the reduction factor of large-scale drifts in heliospheric magnetic field by comparing two sets of simulations: turbulence simulations, where the Parker spiral magnetic field was overlaid by a composite turbulent magnetic field as described by T. Laitinen et al. (2023a), and scatter simulations where the particles propagate in the Parker spiral and experience ad hoc scattering (M. S. Marsh et al. 2013). Our results indicate that turbulence does reduce the large-scale drifts of CRs in the inner heliosphere, particularly at lower energies. The 10 MeV proton drift was reduced to 21% of the nonturbulent drifts ($f_s = 0.21$) for moderate interplanetary turbulence conditions (B+ polarity), whereas for higher energies of 100 and 1000 MeV, the drift reduction coefficients are 0.66 and 0.92, respectively. The drift reduction also depended strongly on the relative amplitude of turbulence: with an increase of turbulence from the level of $dB^2/B^2 = 0.2-2$ (as defined at 1 au heliocentric distance), the reduction factor f_s for 100 MeV protons decreased from 0.91 to 0.23.

We also compared our results to earlier work on drift reduction. Before delving into details of the comparison, it should be noted that our work differs from previous work in two important aspects. First, our magnetic field is not constant, but varies in colatitude and in radial distance. Thus, the theoretical drift velocity of the particles varies depending on the location of the particles. Second, the turbulence model parameters, such as the spectral shape, amplitude, and the turbulence geometry, differ between our and previous work.

Let us first consider the spatial variation of the magnetic field. Most previous modeling work has concentrated on investigating the drift reduction using full-orbit simulations of particles in homogeneous, constant-background magnetic field (e.g., J. Giacalone 1999; J. Candia & E. Roulet 2004; R. C. Tautz & A. Shalchi 2012). In this configuration, there are no macroscopic drifts as there are no macroscopic gradients and curvatures in the magnetic field. Rather than analyzing a macroscopic drift of particles across the mean field, these works have investigated the quantity $\langle v_i \Delta r_i \rangle$, where v_i and Δr_i are velocity and spatial deviation components i and i normal to the background magnetic field, respectively, which equals the diffusion tensor element κ_{ij} , as given by J. Giacalone (1999). It is not clear to the authors of this paper how applicable a drift reduction coefficient calculated from a theoretical starting point without macroscopic drifts is when macroscopic drifts are present.

The only work known to us that does investigate drifts using full-orbit simulations in nonhomogeneous magnetic field is J. Minnie et al. (2007), who introduce a gradient normal to the mean magnetic field. With such a configuration, they were able to quantify the drift velocity and its dependence on turbulence amplitude and particle energy. Unfortunately, they only investigate two particle energies, parameterized by the ratio of the particle Larmor radius and the slab breakpoint scale, $r_L/\lambda_{b\parallel}$. For those values, at $dB^2/B^2=1$, their drift reduction coefficients as defined from the drift velocity in their simulations are 0.33 and 0.85 for $r_L/\lambda_{b\parallel}=0.1$ and 1, respectively. It is interesting to note that inclusion of the gradient in J. Minnie et al. (2007) does not seem to affect the drift coefficient calculated with $\langle v_i \Delta r_j \rangle$, as shown in their Figures 4 and 5.

The second issue to note is the differences in turbulence spectra used by the various simulation studies. As discussed

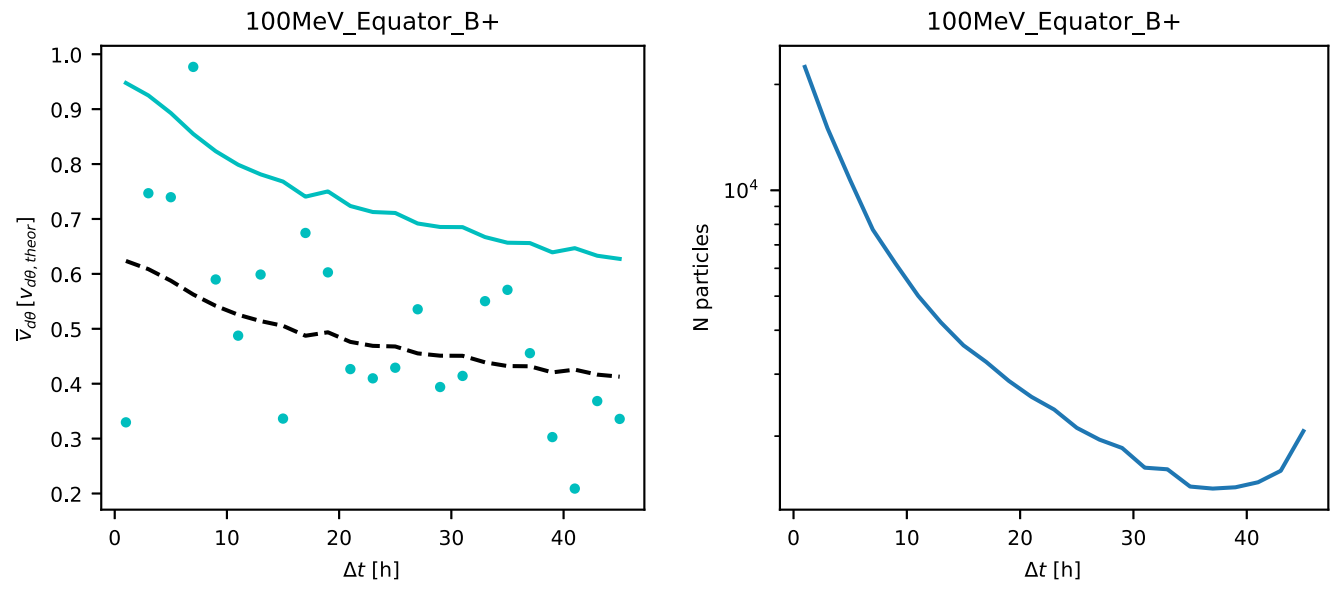


Figure 4. (a) $v_{d\theta}$, in units of $v_{d\theta,\text{theor}}$, of 100 MeV protons (simulation set 4) as a function of Δt , with symbols showing the turbulence simulations and the cyan line the scatter simulations. The dashed black line shows the result of fitting Equation (18). (b) The number of particles corresponding to $v_{d\theta,\text{scat}}$ in (a), used as weights for fitting Equation (18).

Table 2
Drift Reduction Factors

Set	$r_L/l_{b\parallel}$	f_s	σ_{fs}	f_s (Bie1997)	f_s (Eng2017)
1	0.0199	0.21	0.13	0.010	0.045
2	0.0199	0.26	0.13	0.010	0.045
3	0.0643	0.91	0.048	0.25	0.90
4	0.0643	0.66	0.052	0.099	0.29
5	0.0643	0.23	0.042	0.032	0.015
6	0.0643	0.71	0.03	0.099	0.29
7	0.245	0.92	0.019	0.61	0.83
8	0.245	0.92	0.021	0.61	0.83

Note. Column (1): the simulation set. Column (2): the ratio of the particle's Larmor radius and the breakpoint scale of the slab component of the turbulence, $r_L/l_{b\parallel}$. Columns (3) and (4): the drift reduction factor and its standard deviation obtained from the simulations. Columns (5) and (6): drift reduction factors calculated with the turbulence and particle parameters using the J. W. Bieber & W. H. Matthaeus (1997, Bie1997)) and N. E. Engelbrecht et al. (2017, Eng2017)) models, respectively. All quantities are calculated at 1 au heliocentric distance.

above, the ratio between the parallel and perpendicular scales, as well as spectral shapes, differ between our study and the study of J. Minnie et al. (2007). Drift reduction simulation studies have used a variety of turbulence parameters and models: J. Giacalone (1999) and J. Candia & E. Roulet (2004) consider isotropic turbulence, whereas R. C. Tautz & A. Shalchi (2012) investigates the drift reduction for slab, 2D, composite, and isotropic turbulence, although for $l_{sl} = l_{2D}$ and a different slab-to-2D energy ratio for their composite model than J. Minnie et al. (2007) and our study. Further, they only sample different energies for the isotropic case. The lack of full sampling of the parameter space is a common shortcoming of all these studies, most likely due to the simulations being very time-consuming. In particular, the energy dependence of the drift reduction has not been well covered by simulation studies for the case of composite turbulence, as can be seen in Figure 6.

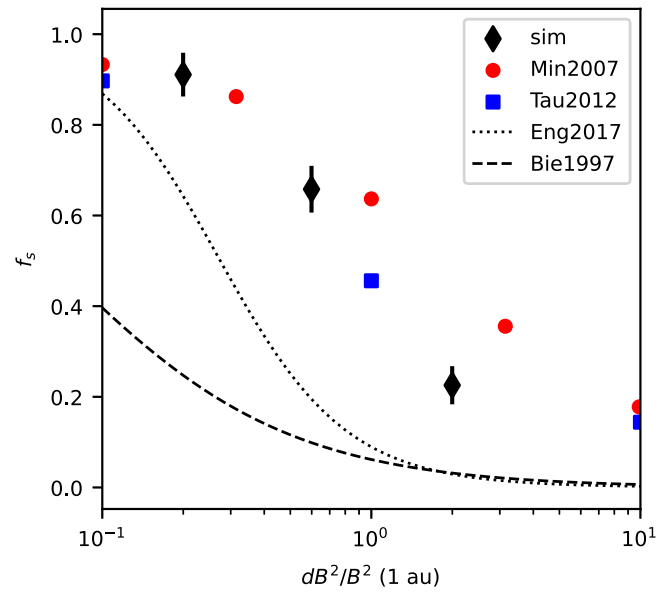


Figure 5. Drift reduction factor for 100 MeV protons as a function of relative turbulence variance, from our simulations (black diamonds) and for the models by J. W. Bieber & W. H. Matthaeus (1997, dashed curves) and N. E. Engelbrecht et al. (2017, dotted curves). The red circles and blue squares are from the J. Minnie et al. (2007) and R. C. Tautz & A. Shalchi (2012) simulations, respectively, with $r_L/\lambda_{b\parallel}=0.1$, corresponding to a proton energy of 227 MeV.

Thus, it is very difficult to draw conclusions from earlier studies of drift reduction, particularly when it comes to the energy dependence of the drift reduction. R. A. Burger & D. J. Visser (2010) derive a parameterized form of the drift reduction coefficient to be used in GCR modulation models using the results of J. Minnie et al. (2007), however they are limited by the two energies included in that study. The theoretical model by N. E. Engelbrecht et al. (2017) shows an improved fit to the J. Minnie et al. (2007) results, as compared to J. W. Bieber & W. H. Matthaeus (1997); however, as shown by J. P. van den Berg et al. (2021), the drift coefficient depends very strongly on which theory is used to derive the

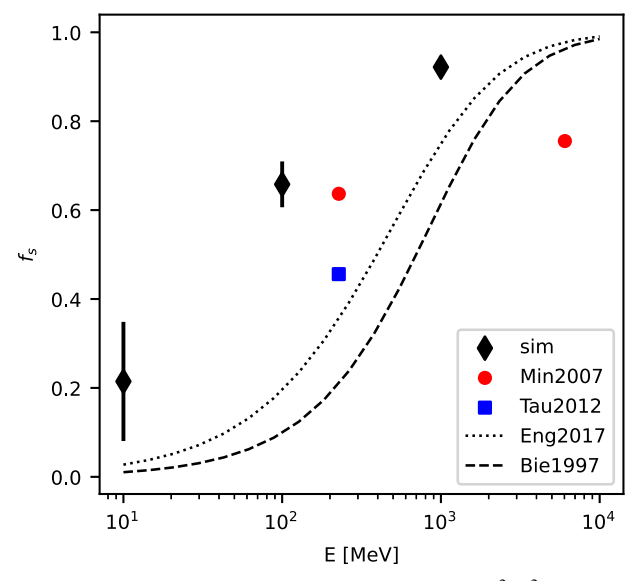


Figure 6. Drift reduction factor for turbulence amplitude $dB^2/B^2 = 0.6$ at 1 au as a function of proton energy, from our simulations (black diamonds) and for the theoretical models of J. W. Bieber & W. H. Matthaeus (1997, dashed curves) and N. E. Engelbrecht et al. (2017, dotted curves). The red circles and blue squares are from the J. Minnie et al. (2007) and R. C. Tautz & A. Shalchi (2012) simulations, respectively, with $dB^2/B^2 = 1$.

perpendicular diffusion coefficient utilized in the N. E. Engelbrecht et al. (2017) approach.

A recent study by N. E. Engelbrecht et al. (2022) showed that the RBD model used in this paper results in larger particle perpendicular mean free paths in the heliosphere than the FLRW (J. R. Jokipii 1966) and nonlinear guiding center (NLGC; W. H. Matthaeus et al. 2003) theories. Thus, our choice to use RBD for the drift reduction coefficient with the N. E. Engelbrecht et al. (2017) approach (Equation (12)) would result in smaller f_s . However, comparison of the relative magnitudes of the RBD, FLRW, and NLGC perpendicular mean free paths is not trivial: In W. H. Matthaeus et al. (2003), the FLRW mean free path was larger than the NLGC one, and D. Ruffolo et al. (2012) found the NLGC mean free path to be larger than the RBD one, both unlike similar comparisons in N. E. Engelbrecht et al. (2022). We believe this may be related to other parameters used in the abovementioned studies, in particular the spectral shape of the turbulence components. For example, the approach of N. E. Engelbrecht et al. (2017) that uses the NLGC theory can be shown to have a $\tau\Omega \propto (l_{sl}/l_{2D})^{2/3}$ dependence; thus, the different values of this parameter, e.g., $l_{sl}/l_{\rm 2D}=10$ for N. E. Engelbrecht et al. (2017), 2 in our study, and 1 in D. Ruffolo et al. (2012), may result in significant differences in the drift reduction factor. Further investigation on the sensitivity of the different perpendicular particle diffusion theories on different parameters is beyond the scope of this paper.

Our results demonstrate a sharp contrast to the predictions of the J. W. Bieber & W. H. Matthaeus (1997) and N. E. Engelbrecht et al. (2017) results. At high energies these predictions are similar to our results, however the energy dependence of our drift reduction factor is significantly weaker than that predicted by theoretical models based on field-line or particle cross-field diffusion coefficients. It is quite possible that the issue is related to how the particle Larmor radius relates to the perpendicular and parallel turbulence scales, as discussed above. We will investigate this further in a forthcoming paper. An upcoming

development is also to include the convective electric field $E = -v_{\rm sw} \times B$, where $v_{\rm sw}$ is the solar wind velocity, in our model. This will enable us to address drifts in longitude, for which the $E \times B$ drift is significant (e.g., J. A. Burns & G. Halpern 1968; S. Dalla et al. 2013).

5. Conclusions

We have investigated the effect of magnetic field turbulence on the large-scale drifts present in the heliospheric magnetic field. As discussed in previous work, turbulence tends to reduce the amount of drift, and this has been characterized via a drift reduction coefficient f_s , which depends on particle properties such as energy and mass-to-charge ratio, and turbulence characteristics. Using test-particle full-orbit simulations, we have for the first time analyzed the drift reduction due to turbulence in a heliospheric context, using our analytic heliospheric turbulence model (T. Laitinen et al. 2023a). We found the following:

- 1. The drift reduction coefficient of protons is energy dependent, with $f_s = 0.2$ for 10 MeV protons in moderate turbulence with $dB^2/B^2 = 0.6$ at 1 au heliocentric distance. At higher energies of 100 MeV and 1000 MeV, the reduction is $f_s = 0.7$ and 0.9, respectively.
- 2. Stronger turbulence, with $dB^2/B^2 = 2$, gives rise to stronger drift reduction, with $f_s = 0.2$ for $100 \,\text{MeV}$ protons, whereas for weaker turbulence, $dB^2/B^2 = 0.2$, the reduction is small, with $f_s = 0.9$.
- 3. Our values of the drift reduction coefficient are similar to those obtained by simulations in constant magnetic field by J. Minnie et al. (2007) and R. C. Tautz & A. Shalchi (2012). However, care should be taken with the comparison as the turbulence and background models differ significantly.
- According to our simulations, the drift reduction is significantly weaker than that proposed by theoretical models by J. W. Bieber & W. H. Matthaeus (1997) and N. E. Engelbrecht et al. (2017), particularly at lower energies.

Thus, we find that while the turbulence does reduce the macroscopic drift in the IMF, the strong reduction predicted by theoretical approaches (J. W. Bieber & W. H. Matthaeus 1997; N. E. Engelbrecht et al. 2017; J. P. van den Berg et al. 2021), particularly at lower energies, is not supported by our simulations. Thus, we expect that the effects of drifts on SEPs remain significant at large ion energies (e.g., >100 MeV protons), particularly for heavier elements which have larger Larmor radii.

Acknowledgments

T.L. and S.D. acknowledge support from the UK Science and Technology Facilities Council (STFC) through grant Nos. ST/V000934/1 and ST/Y002725/1. This work was performed using resources provided by the Cambridge Service for Data Driven Discovery (CSD3) operated by the University of Cambridge Research Computing Service (www.csd3.cam.ac.uk), provided by Dell EMC and Intel using Tier-2 funding from the Engineering and Physical Sciences Research Council (capital grant EP/P020259/1), and DiRAC funding from the Science and Technology Facilities Council (www.dirac.ac.uk).

Data Availability

The simulation data used in this study are available as CSV files via Zenodo at doi: 10.5281/zenodo.14284455. Electronic versions of Tables 1 and 2 are also provided in CSV format.

Appendix A Turbulence Parameters

Our simulations use the same turbulence parameters as T. Laitinen et al. (2023a), aside from the turbulence amplitude, which is varied, as given in column (7) of Table 1. The other parameters are briefly presented here for the reader's convenience.

The turbulence generation is based on a superposition of Fourier modes logarithmically equispaced in wavenumber k, using the approach by J. Giacalone & J. R. Jokipii (1999). We use a 2D-slab composite model with separate spectra for the 2D (k_\perp) and slab (k_\parallel) components, with the power in the two components divided as 80%:20%. The power spectra consists of a large-scale k^p component, with p=0, at wavenumbers below the breakpoint scales $l_{c\perp}$ and $l_{c\parallel}$, respectively (note that we use l_c here instead of λ_c as used by T. Laitinen et al. 2023a in order to avoid confusion with the parallel scattering mean free path λ_\parallel). At higher wavenumbers, we use a Kolmogorov spectrum with power-law index 8/3 and 5/3 for the 2D and slab components, respectively. The breakpoint scales are defined as $l_{c\perp}=0.04~(r/r_\odot)^{0.8}~r_\odot$, where r is the heliocentric distance and r_\odot is the solar radius, and $l_{c\parallel}=2l_{c\perp}$. Finally, the total amplitude of the turbulence, δB , varies with location as $\delta B^2 \propto r^{-3.3}$, with $\delta B^2/B^2=0.03$ at r_\odot , where B is the background magnetic field given by Equation (13).

For further information about the parameters, their sources, and how they are used in the model, we refer the reader to the full description of the model in T. Laitinen et al. (2023a).

Appendix B Theoretical Drift Velocity at 1 au

The pitch-angle-dependent drift velocity in colatitude due to magnetic field gradient and curvature in the Parker spiral is given by S. Dalla et al. (2013) as

$$v_{d\theta, \text{theor}} = A \frac{\gamma m}{a} \left(\frac{1}{2} v_{\perp}^2 + v_{\parallel}^2 \right) f(r, \theta), \tag{B1}$$

where

$$f(r,\theta) = \frac{a}{B_0 r_0^2} \frac{x^2 (x^2 + 2)}{(x^2 + 1)^2},$$
 (B2)

with $x = r/a(\theta)$ and $a(\theta) = v_{\rm sw}/(\Omega \sin \theta)$, and where A is the sign of the Parker spiral magnetic field, as in Equation (13). Note that S. Dalla et al. (2013) show the drift rate in latitude rather than colatitude, hence their sign of $v_{d\theta}$ is opposite to ours. Our model is also unipolar unlike S. Dalla et al. (2013), who used a bipolar magnetic field, hence we do not incorporate the change of the sign of the drift velocity at the equator, $\operatorname{sgn}\left(\frac{\pi}{2} - \theta\right)$ in Equation (B1).

To evaluate the representative value of the drift velocity, we average Equation (B1) over the particle velocity distribution, assuming an isotropic pitch-angle distribution. The isotropy assumption is justified by the fact that, for our simulation cases, the scattering timescale at 1 au has values between ~500 and 2000 s, which are short compared to the timescales relevant to the determination of the drift velocity. Following the pitch-angle averaging, the terms in the parentheses in Equation (B1) become

$$\frac{\overline{1}v_{\perp}^{2}+v_{\parallel}^{2}}{2}=\frac{2}{3}v^{2}.$$

In our simulations, we characterize the Parker spiral with solar wind speed $v_{\rm sw} = 400 \, {\rm km \ s^{-1}}$. Further, our region of interest is at the solar equator, with $\theta = 90^{\circ}$, for which the factor

$$f(r, \theta) = \frac{a_{\text{eq}}}{B_0} \frac{r^2}{r_0^2} \frac{r^2 + 2a_{\text{eq}}^2}{(r^2 + a_{\text{eq}}^2)^2},$$

where $a_{\rm eq} = a(\theta = 90^{\circ}) \approx 0.93$ au, and the drift velocity

$$v_{d\theta,\text{theor}} = \frac{2}{3} A \ a \ r_{L0} \ v \frac{r^2}{r_0^2} \frac{r^2 + 2a_{\text{eq}}^2}{(r^2 + a_{\text{eq}}^2)^2}, \tag{B3}$$

where r_{L0} is the particle Larmor radius at magnetic field B_0 . This can also be written in terms of the Larmor radius of the particle at 1 au as

$$v_{d\theta,\text{theor}} = \frac{2}{3} A r_L v \frac{r^2 + 2a_{\text{eq}}^2}{(r^2 + a_{\text{eq}}^2)^{3/2}},$$
 (B4)

Using this $v_{d\theta,\text{theor}}$, the deviation in colatitude in the time interval Δt at distance r would be expected to be

$$\Delta \theta = \frac{v_{d\theta} \Delta t}{r}.$$
 (B5)

We demonstrate this in Figure 7, where panel (a) shows the theoretical drift velocity in kilometers per second, and panel (b) in angular units, for the parameters shown in this study.

It is important to note that in our simulations the particle's location will have deviated from r=1 au between its first and last crossing of the 1 au sphere. As discussed in S. Dalla et al. (2013) and shown in Figure 7(a), the theoretical drift velocity due to the curvature and gradient tends toward a constant value at large distances, $r \gg a$. Thus, as a consequence r in the denominator of Equation (B5), the deviation in colatitude, for a given Δt , decreases at small and large heliocentric distances, as shown in Figure 7(b). Therefore, a particle that propagates at a wide range of heliocentric distances between its first and last crossing of the 1 au sphere will have drifted with smaller (angular) drift velocity on average than a particle that would have remained at 1 au.

For this reason, the drift velocity defined in Equation (16) can be expected to be smaller than $v_{d\theta,\text{theor}}$ for a particle that has propagated to small or large heliospheric distances before returning to 1 au.

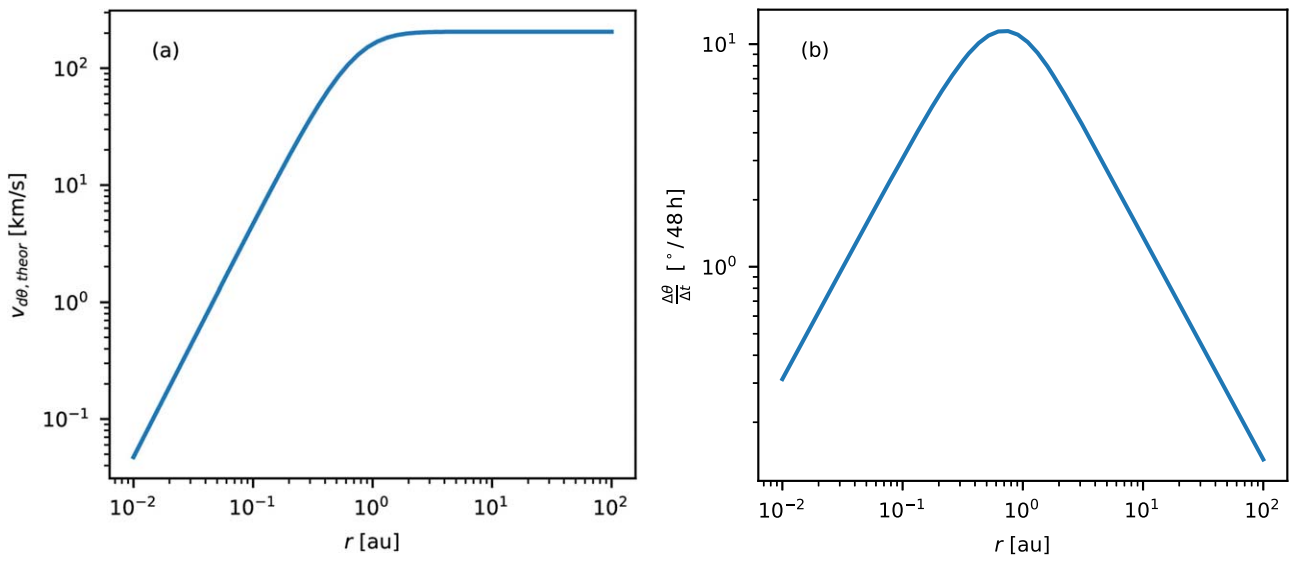


Figure 7. The theoretical drift velocity in heliolatitude, $v_{d\theta,\text{theor}}$, of 100 MeV protons in units of (a) kilometers per second, and (b) Angular units as a function of heliocentric distance in the heliospheric equatorial plane, for the solar wind speed and Parker spiral magnetic field strength used in this study.

ORCID iDs

- T. Laitinen https://orcid.org/0000-0002-7719-7783
- S. Dalla https://orcid.org/0000-0002-7837-5780

References

```
Battarbee, M., Dalla, S., & Marsh, M. S. 2017, ApJ, 836, 138
Battarbee, M., Dalla, S., & Marsh, M. S. 2018, ApJ, 854, 23
Bieber, J. W., & Matthaeus, W. H. 1997, ApJ, 485, 655
Burger, R. A., & Visser, D. J. 2010, ApJ, 725, 1366
Burns, J. A., & Halpern, G. 1968, JGR, 73, 7377
Candia, J., & Roulet, E. 2004, JCAP, 2004, 007
Chhiber, R., Subedi, P., Usmanov, A. V., et al. 2017, ApJS, 230, 21
Dalla, S., & Browning, P. K. 2005, A&A, 436, 1103
Dalla, S., Marsh, M. S., Kelly, J., & Laitinen, T. 2013, JGRA, 118, 5979
Dalla, S., Marsh, M. S., & Laitinen, T. 2015, ApJ, 808, 62
Engelbrecht, N. E., Effenberger, F., Florinski, V., et al. 2022, SSRv,
Engelbrecht, N. E., Strauss, R. D., Roux, J. A., & Burger, R. A. 2017, ApJ,
   841, 107
Forman, M. A., Jokipii, J. R., & Owens, A. J. 1974, ApJ, 192, 535
Ghilea, M. C., Ruffolo, D., Chuychai, P., et al. 2011, ApJ, 741, 16
Giacalone, J., & Jokipii, J. R. 1999, ApJ, 520, 204
Giacalone, J., Jokipii, J. R., & Kóta, J. 1999, ICRC (Salt Lake City, UT), 7, 37
Gleeson, L. J. 1969, P&SS, 17, 31
```

```
Green, M. S. 1951, JChPh, 19, 1036
Jokipii, J. R. 1966, ApJ, 146, 480
Jokipii, J. R., Levy, E. H., & Hubbard, W. B. 1977, ApJ, 213, 861
Kubo, R. 1957, JPSJ, 12, 570
Laitinen, T., Dalla, S., Waterfall, C. O. G., & Hutchinson, A. 2023a, ApJ,
  943, 108
Laitinen, T., Dalla, S., Waterfall, C. O. G., & Hutchinson, A. 2023b, A&A,
  673, L8
Marsh, M. S., Dalla, S., Kelly, J., & Laitinen, T. 2013, ApJ, 774, 4
Matthaeus, W. H., Qin, G., Bieber, J. W., & Zank, G. P. 2003, ApJL,
  590, L53
Matthaeus, W. H., Smith, C. W., & Bieber, J. W. 1999, in AIP Conf. Ser. 471,
  Solar Wind Nine, ed. S. R. Habbal et al. (Melville, NY: AIP), 511
Minnie, J., Bieber, J. W., Matthaeus, W. H., & Burger, R. A. 2007, ApJ,
  670, 1149
Parker, E. N. 1958, ApJ, 128, 664
Parker, E. N. 1965, P&SS, 13, 9
Potgieter, M. S., Le Roux, J. A., & Burger, R. A. 1989, JGR, 94, 2323
Rossi, B., & Olbert, S. 1970, Introduction to the Physics of Space (New York:
  McGraw-Hill)
Ruffolo, D., Pianpanit, T., Matthaeus, W. H., & Chuychai, P. 2012, ApJL,
  747, L34
Tautz, R. C., & Shalchi, A. 2012, ApJ, 744, 125
Taylor, G. I. 1922, PLMS, s2, 196
van den Berg, J. P., Engelbrecht, N. E., Wijsen, N., & Strauss, R. D. 2021, ApJ,
Virtanen, P., Gommers, R., Oliphant, T. E., et al. 2020, NatMe, 17, 261
```